

## Research Article

# Green synthesised ZnO/CuO nanocomposites for energy storage, environmental remediation and optoelectronic applications

Sahana Nagarakere Chandranna<sup>a</sup>, Vinayakprasanna N Hegde<sup>b,\*</sup>, N C Sandhya<sup>c</sup>, B C Hemaraju<sup>d</sup>, Pradeep T M<sup>e</sup>

<sup>a</sup> Department of Studies in Environmental Science, University of Mysore, Manasagangothri, Mysuru 570006, India

<sup>b</sup> Department of Physics, Vidyavardhaka College of Engineering, Mysuru 570002, India

<sup>c</sup> Department of Chemistry, Mysore University School of Engineering, Mysuru 570006, India

<sup>d</sup> Department of Physics, Malnad College of Engineering, Hassan 573202, India

<sup>e</sup> Department of Electronics and Communication Engineering, GM University, Davangere 577006, India

## ARTICLE INFO

## Keywords:

ZnO/CuO  
 Nanocomposite  
 Energy  
 Optoelectronics  
 Photocatalytic

## ABSTRACT

Zinc oxide/Copper oxide (ZnO/CuO) nanocomposites (NCs) have gained substantial importance due to their synergistic structural, electrical, optical and photocatalytic properties. In this study, ZnO/CuO NCs were synthesized using a green solution combustion method with lemon extract as fuel. X-ray diffraction (XRD) confirmed the formation of highly crystalline ZnO and CuO phases, while scanning electron microscopy (SEM) revealed an agglomerated morphology. UV-visible (UV-Vis) spectroscopy indicated an optical bandgap of 3.27 eV and photoluminescence (PL) analysis demonstrated strong near-band-edge and defect-related emissions. Dielectric studies highlighted superior charge storage capabilities, making these materials promising for energy storage applications. Photocatalytic investigation on crystal violet dye degradation under visible light showed an 83% efficiency at neutral pH, emphasizing their environmental remediation potential. The ZnO/CuO heterostructure facilitates enhanced charge separation and light absorption, boosting performance in opto-electronic devices. This study provides a comprehensive evaluation of ZnO/CuO NCs, positioning them as multifunctional materials for sustainable energy, environmental and technological applications.

## 1. Introduction

Nanostructured materials are attracting significant interest because of their distinctive characteristics and wide range of potential uses. ZnO, a wide bandgap semiconductor and CuO, a narrow bandgap semiconductor, represent a promising combination for the development of nanocomposites with enhanced functional properties. ZnO is widely recognized for its high exciton binding energy, environmental stability and strong optical absorption, making them well-suited for applications in photocatalysis, opto-electronics and energy storage [1,2]. However, their practical application is often limited by the fast recombination of photogenerated electron-hole pairs [3]. On the other hand, CuO, with its p-type conductivity and narrow bandgap, not only enhances charge separation when combined with ZnO but also extends light absorption into the visible spectrum [4]. This complementary behaviour forms the basis for designing ZnO/CuO NCs with superior performance in various fields.

The ZnO/CuO NCs have shown remarkable potential in diverse areas. In energy storage, these materials exhibit high dielectric constants

and conductivity, making them suitable for capacitors and battery components [5]. Their photocatalytic capabilities are particularly noteworthy in environmental remediation, where they effectively degrade organic pollutants and dyes under UV-visible light [6]. In solid-state lighting, the luminescence properties of these composites are leveraged to enhance the efficiency and lifespan of light-emitting diodes (LEDs). Furthermore, ZnO/CuO NCs have been explored as gas sensors, detecting toxic gases like ammonia and ethanol due to their enhanced sensitivity and selectivity [7]. Their broad utility positions these NCs as pivotal materials in advancing sustainable technologies. Recent studies have highlighted the synergistic properties of ZnO and CuO in nanocomposite systems. Chang et al. [8] synthesized ZnO/CuO NCs via a hydrothermal method and reported a sixfold enhancement in the photocatalytic degradation rate of methylene blue (MB) when compared to pure ZnO. This improvement was ascribed to efficient charge-transfer and reduced recombination rates. Similarly, Saravanan et al. [9] demonstrated the superior gas-sensing and photocatalytic performance of ZnO/CuO composites prepared via thermal decomposition. They emphasized the role of CuO in narrowing the bandgap and increasing light absorption in

\* Corresponding author.

E-mail address: [vinayak.phy@vnce.ac.in](mailto:vinayak.phy@vnce.ac.in) (V.N. Hegde).

<https://doi.org/10.1016/j.chphma.2025.10.002>

Received 2 August 2025; Received in revised form 28 September 2025; Accepted 8 October 2025

Available online 16 October 2025

2772-5715/© 2025 The Authors. Publishing Services by Elsevier B.V. on behalf of KeAi Communications Co. Ltd. This is an open access article under the CC BY-NC-ND license (<http://creativecommons.org/licenses/by-nc-nd/4.0/>)

the visible region. Shinde et al. [10] explored ZnO/CuO NCs as effective photocatalysts and gas sensors, achieving nearly 90% degradation of dye under optimized conditions. The researchers also highlighted the importance of structural and optical characterization in understanding the material's behaviour.

Although significant advancements have been achieved in the synthesis and characterization of ZnO/CuO NCs, most research has primarily focused on their individual properties. Comprehensive studies exploring the combined structural, dielectric, optical and luminescence characteristics—and their corresponding applications—are still limited. This work seeks to bridge that gap by employing a simple and cost-effective synthesis approach to develop ZnO/CuO NCs and systematically investigate their multifunctional properties. Unlike previous works that predominantly focused on either photocatalysis or gas sensing, this research emphasizes the interplay between structural, electronic and optical properties, providing a holistic understanding of their potential in energy storage, solid-state lighting and environmental remediation. The ZnO/CuO nanocomposite system offers a versatile platform for addressing challenges in energy, lighting and environmental sustainability. By leveraging the complementary properties of ZnO and CuO, this study advances our understanding of these materials and places the groundwork for their application in next-generation technologies.

## 2. Experimental details

ZnO/CuO (1:1) NCs were synthesized using the solution combustion method with lemon extract (citric acid) as a green fuel. The synthesis protocol was adapted from [6], with slight modifications in the precursor ratio and calcination conditions. In this process, zinc nitrate and copper nitrate serve as the precursors for ZnO and CuO, respectively. Lemon extract, rich in citric acid and organic compounds, acts as both a fuel and a complexing agent, enhancing combustion efficiency and uniform mixing of the precursors. The extract was prepared from fresh lemon juice obtained from locally available citrus limon fruits. The juice was filtered to remove pulp and seeds, and the clear extract was used directly in the combustion synthesis. Citric acid is the major active component, but the extract also contains minor amounts of ascorbic acid, sugars, flavonoids, and trace minerals, which can serve as mild reducing and stabilizing agents during nanoparticle formation. Stoichiometric quantities of the precursor salts are dissolved in 20 mL deionized water, after which 10 mL of lemon extract is added to obtain a uniform solution. This mixture is then subjected to heating in a muffle furnace at approximately 500 °C for 10 min, triggering a self-propagating combustion reaction that produces a fluffy powder. The obtained product is subsequently calcined at 800 °C for 3 h to eliminate any remaining organic content and to achieve phase purity.

The synthesized ZnO/CuO NCs were characterized using XRD (Rigaku-Altima-4), SEM (ZEISS Evo-15), UV-visible spectroscopy (Perkin-Elmer Lambda-35), Fourier transform infrared (FTIR) spectroscopy (BRUKER IFS 66 V), photoluminescence (Hitachi F-4600) and dielectric properties (NF LCR meter) were employed to study their structural, morphological, optical and dielectric properties.

Crystal violet (CV) was chosen as a model organic dye to evaluate the photocatalytic activity of ZnO/CuO NCs. A stock CV solution ( $1.0 \times 10^{-3}$  M) was prepared by dissolving 0.0373 g of dye in 100 mL of doubly distilled water. Working solutions with concentrations ranging from 0 to 1.0 mg/L were obtained by appropriate dilution. For each photocatalytic experiment, 10 mg of ZnO/CuO NCs was dispersed in 100 mL of the dye solution. The initial pH of the solution was measured with a digital pH meter (Systronics Model 335) and adjusted, when necessary, using 0.05 mol/L  $H_2SO_4$  to achieve optimal photocatalytic conditions.

The suspension was irradiated with a 200 W tungsten lamp, with a circulating water layer placed in front of the lamp to filter infrared radiation and minimize heating effects. At 15 min intervals, 3 mL aliquots were withdrawn, centrifuged to remove catalyst particles and the absorbance of the supernatant was recorded at 650 nm using a UV-Vis

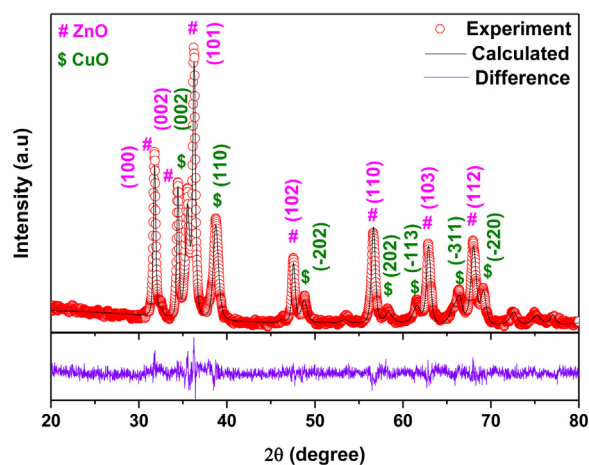


Fig. 1. XRD profile of ZnO/CuO NCs.

spectrophotometer (Systronics Model 106). Control experiments were carried out under identical conditions without catalyst and without dye to account for baseline effects. The degradation efficiency and absolute dye concentrations were calculated from the absorbance values to evaluate photocatalytic kinetics and saturation behaviour.

## 3. Results and discussion

### 3.1. Structural analysis

Fig. 1 presents the Rietveld refined XRD pattern of the ZnO/CuO NCs. The refinement was carried out using Profex software [11], through a structured, step-by-step approach. Initially, the XRD data was imported, and phase identification was performed using the integrated search-match module. The Fundamental Parameters Approach (FPA) was utilized for profile fitting, enabling precise modelling of the diffraction pattern. Key parameters such as crystallite size, lattice constants, and micro-strain were iteratively refined to closely match the calculated profile with the experimental data. Refinement was continued until satisfactory values for the goodness of fit (GoF) and chi-square ( $\chi^2$ ) were obtained, indicating a reliable correlation between the observed and simulated patterns. Quantitative phase analysis of the XRD data was performed by Rietveld refinement. The refined phase fractions are ZnO = 52.6 wt% and CuO = 47.4 wt%, confirming the near 1:1 molar ratio between ZnO and CuO in the final nanocomposite, consistent with the intended synthesis design. Atomic positions and profile parameters converged with small estimated standard deviations (ESD = 0.0056), confirming the quality of the fit. The resulting refinement and structural parameters are presented in Table 1.

The XRD patterns of the ZnO/CuO NCs exhibit sharp and well-defined peaks, confirming a high degree of crystallinity in the synthesized sample. The obtained diffraction peaks were indexed to the standard JCPDS card No. 36-1451 for ZnO (hexagonal-wurtzite phase) and card No. 89-5899 for CuO (monoclinic phase). Peaks corresponding to ZnO were marked with a “#”, while those of CuO were denoted with a “\$”.

The absence of any additional peaks indicates the successful synthesis of ZnO and CuO phases without detectable impurities or residual bulk precursors, further validating the purity of the NCs. The diffraction peaks at 31.87°, 34.46°, 35.93°, 47.66°, 56.67°, 62.84°, and 68.04° correspond to the (100), (002), (101), (102), (110), (103), and (112) planes of the hexagonal wurtzite ZnO phase. Similarly, the peaks at 38.76°, 48.76°, 58.37°, 61.54°, 66.28°, and 69.20° belong to the (002), (110), (-202), (202), (-113), (-311), and (-220) planes of the monoclinic CuO phase.

**Table 1**  
Refinement parameters and structural properties of ZnO/CuO NCs.

Phase	Phase fractions (wt%)	$D_{\text{Scherrer}}$ (nm)	$D_{\text{W-H}}$ (nm)	$\epsilon$	GoF	$\chi^2$
ZnO	52.6	20.8	35	$1.8 \times 10^{-3}$	1.08	1.17
CuO	47.4	19.1	20.7	$0.45 \times 10^{-3}$		

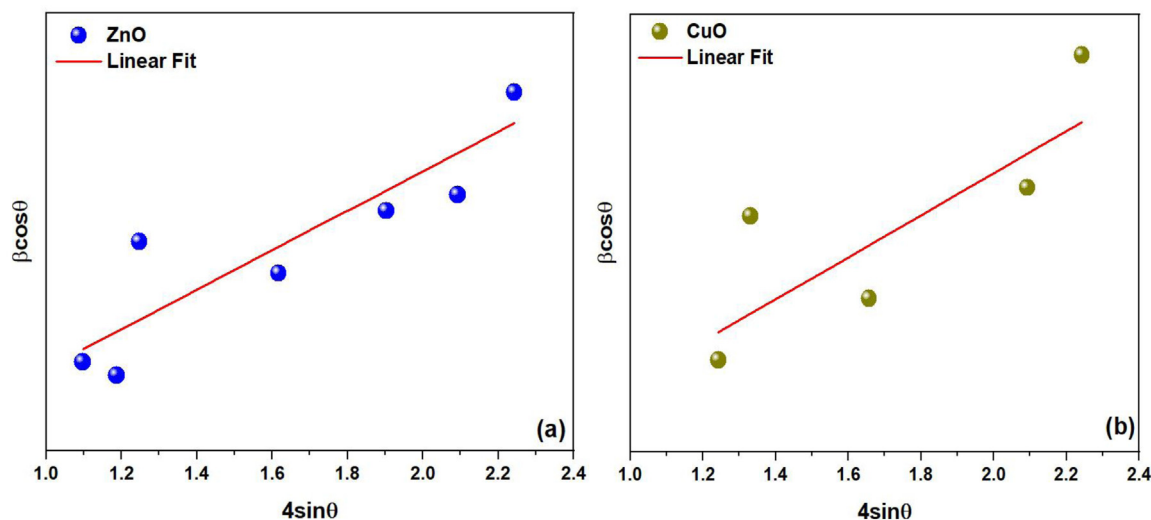


Fig. 2. W-H plot of (a) ZnO and (b) CuO phases in ZnO/CuO NCs.

The crystallite size ( $D$ ) of the ZnO/CuO NCs was determined using the Scherrer equation [12].

$$D = k\lambda/\beta\cos\theta, \quad (1)$$

where  $k$  is the Scherrer constant,  $\lambda$  is the wavelength of the X-ray,  $\beta$  is the full width at half maximum (FWHM) of the peak. The average  $D$  for ZnO and CuO phases were calculated from the respective major peaks, was found to be 20.8 and 19.1 nm respectively. The sharpness and intensity of the peaks suggest excellent crystallinity in the ZnO/CuO NCs, which is beneficial for applications requiring high structural order. The absence of spurious peaks confirms the phase purity of the composite. This ensures that the properties of the nanocomposite are intrinsic to the ZnO and CuO phases, without interference from impurities. The observed variation in peak intensities corresponds to the preferential orientation of crystallites along specific planes. The prominent (100) peak for ZnO indicates a preferred orientation along the  $a$ -axis, often associated with enhanced optical and electronic properties. The coexistence of ZnO and CuO phases without detectable impurity phases suggests minimal interaction at the atomic scale, maintaining the individual properties of ZnO and CuO. This feature is advantageous for applications in photocatalysis, sensors, and optoelectronic devices where a synergistic effect between phases is desired. The prepared ZnO/CuO NCs are polycrystalline in nature, as confirmed by both XRD and SEM analyses. While the Scherrer method provides an estimate of  $D$ , it does not account for the strain ( $\epsilon$ ) induced broadening of diffraction peaks. To achieve a more comprehensive understanding of the microstructural properties, the Williamson–Hall (W-H) method was considered, which considers both the  $D$  and  $\epsilon$  contributions to the broadening [13].

$$\beta\cos\theta = \frac{0.9\lambda}{D} + 4\epsilon\sin\theta. \quad (2)$$

A plot of  $\beta\cos\theta$  versus  $4\sin\theta$ , known as the W-H plot, is used to estimate both  $D$  and  $\epsilon$ . The W-H plot for ZnO and CuO are shown in Fig. 2. The intercept of the linear fit corresponds to the crystallite size, while the slope provides the lattice strain. The calculated  $D$ s were 35 nm for ZnO and 20.7 nm for CuO, indicating that CuO crystallites are relatively finer compared to ZnO within the composite matrix. The corresponding

lattice strains were estimated as  $1.8 \times 10^{-3}$  for ZnO and  $0.45 \times 10^{-3}$  for CuO, suggesting that both phases possess a well-ordered crystal lattice with minimal microstructural distortion. The lower strain in CuO implies that the CuO crystallites experience less internal stress, while ZnO exhibits slightly higher lattice strain, likely due to lattice mismatch and interfacial stress between the ZnO and CuO domains. These values are consistent with the sharp diffraction peaks observed in the XRD pattern, confirming good crystallinity of both phases.

### 3.2. Morphology

The morphology and purity of the prepared NCs were analysed by SEM and EDX studies. The SEM image, EDX spectrum, elemental mapping are given in Figs. 3(a)–(e). The SEM image shows a distribution of irregularly shaped particles of varying sizes. Most particles are clustered together, with clear boundaries visible between individual particles, indicating a granular or agglomerated nature. The particles exhibit a range of sizes, from smaller submicron particles to larger micrometer-scale aggregates. The irregular particle shapes suggest that the synthesis method produced a polycrystalline material with no significant preferential growth directions. Clustering of particles can be observed, likely due to Van der Waals forces or other weak interactions between particles [14]. This agglomeration is common in nanoparticles and micro-scale materials due to their high surface energy. The surface texture appears rough and porous, which could enhance properties such as surface area and catalytic activity. Such a morphology is advantageous for applications like photocatalysis, sensors, and energy storage, as it promotes better interaction with surrounding media (reactants, ions, or light). While the particles appear uniform in texture, their size distribution suggests some degree of polydispersity. Energy dispersive X-ray (EDX) spectrum of ZnO/CuO NCs shown in Fig. 3(b) confirms the purity of the prepared sample. It exhibits only peaks for Zn, Cu and O. EDX elemental mapping presented in Figs. 3(c)–(e), confirms the uniform spatial distribution of Zn, Cu, and O across the scanned region. The mapping images show evenly scattered signals for both Zn and Cu without localized agglomeration, suggesting good phase mixing and compositional homogeneity of

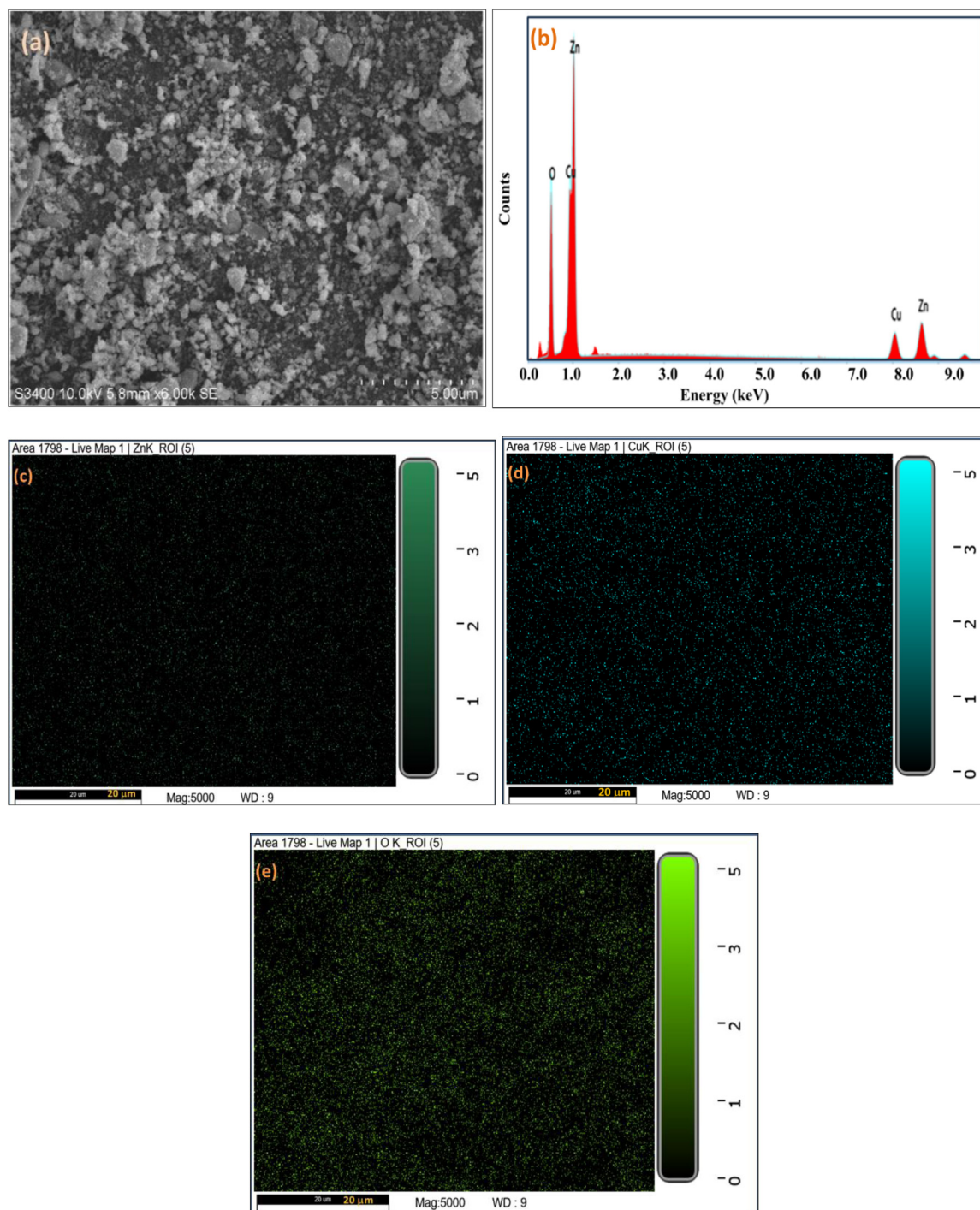


**Fig. 3.** (a) SEM image and (b) EDX spectrum of ZnO/CuO NCs and (c)–(e) elemental mapping of Zn, Cu and O respectively.

the ZnO/CuO nanocomposites. Quantitative EDX analysis further verified that the measured atomic percentages are consistent with the nominal stoichiometry. The elemental analysis provides approximately 48.2 at% Zn, 24.6 at% Cu, and 27.2 at% O, consistent with the stoichiometry expected for a 1:1 ZnO/CuO composite. The absence of other elements verified the phase purity of the sample.

### 3.3. FTIR analysis

FTIR spectroscopy was employed to identify functional groups, and possible impurities present in the nanocomposite. This technique

is highly sensitive to vibrational modes of chemical bonds, allowing detection in both crystalline and amorphous phases, as well as surface-adsorbed species. Broad absorption bands observed in the 3200–3500  $\text{cm}^{-1}$  region correspond to the O–H stretching vibrations, indicating the presence of surface hydroxyl groups—a common feature in metal oxide nanostructures due to their high surface area. Peaks in the 2900–3000  $\text{cm}^{-1}$  range are attributed to C–H stretching vibrations, suggesting the presence of residual organic species, likely originating from the synthesis precursors. The absorption band near 1900  $\text{cm}^{-1}$  is corresponds to C=C stretching, which may result from atmospheric carbon contamination. Vibrations in the 1000–1700  $\text{cm}^{-1}$  region correspond to C–O

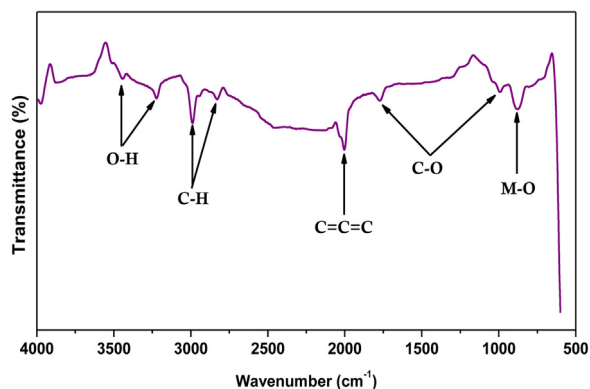


Fig. 4. FTIR spectrum of ZnO/CuO NCs.

$E_g$ (eV)	3.27
$n$	2.30
$\chi$	0.39

bond stretching, possibly due to adsorbed  $\text{CO}_2$ . A distinct peak around  $880\text{ cm}^{-1}$  is assigned to Zn–O and Cu–O stretching modes, which are in good agreement with reported values for ZnO/CuO composites [Fig. 4] [15].

### 3.4. UV–Vis analysis

The UV–visible reflectance spectrum of the ZnO/CuO NCs was recorded in the wavelength range of 250 to 700 nm, as illustrated in Fig. 5(a). The spectrum reveals a prominent absorption peak at 297 nm. The optical band gap ( $E_g$ ) was estimated using the relation  $E_g = hc/\lambda$ ,  $h$  is the Planck’s constant,  $c$  is the speed of light and  $\lambda$  is the wavelength corresponding to the maximum absorption. Additionally, the band gap was further evaluated using the Tauc plot method shown in Fig. 5(b), yielding a value of approximately 3.27 eV. The determined bandgap is matching well with literature [8,16].

The refractive index ( $n$ ) is a critical optical parameter, particularly for semiconductors intended for integration into photonic devices such as optical modulators, switches and filters [17]. In such devices, precise control over  $n$  is essential for efficient light manipulation. ZnO/CuO NCs are especially promising for these applications due to their unique optical and electronic characteristics. Equally important is the evaluation of optical susceptibility ( $\chi$ ), which provides valuable insight into the electronic structure and bonding nature within semiconductor materials. The optical susceptibility reflects how a material responds to an external electro-magnetic (EM) field, thus playing a key role in understanding and engineering optical responses for various applications—including optical communication and optoelectronics. To better understand the optical behaviour of the ZnO/CuO NCs, efforts were made to calculate the  $n$ ,  $\chi$  and absorption coefficient ( $\alpha$ ) using the following expressions [18].

$$(n^2 + 2)^2 (E_g - 0.365) = 154, \quad (3)$$

$$\chi = 0.08 \times \left\{ \left[ -\ln(0.027E_g) \right]^2 - 1 \right\}. \quad (4)$$

The obtained results were tabulated in Table 2.

### 3.5. Photoluminescence analysis

PL spectrum shown in Fig. 6(a) was studied at an excitation wavelength of 325 nm to examine their electronic structure, defect states, and

optical properties. PL spectrum exhibits two peaks at 425 and 555 nm. Peak at 425 nm is due to near-band-edge (NBE) emission of ZnO [16]. The NBE emission arises from the recombination of free excitons or bound excitons. The sharpness and intensity of this peak indicate the dominance of radiative recombination, suggesting a low density of defects in the ZnO matrix [19]. The green emission (peak at 555 nm) is generally attributed to deep-level defects, such as oxygen vacancies ( $V_O$ ), zinc interstitials ( $Zn_i$ ), or Cu-related defect states introduced by CuO in the nanocomposite [15]. The CuO phase can introduce additional defect states, including  $\text{Cu}^+/\text{Cu}^{2+}$  ion traps, which may contribute to this emission [15]. This peak reflects the interaction between ZnO and CuO and their combined defect structure. The intensity of the 425 nm peak compared to the 555 nm peak gives an idea about the quality of the composite and the degree of defect density. A higher 425 nm peak relative to the 555 nm peak indicates a higher crystallinity and fewer defects. The broader emission bands suggest a distribution of defect states, implying that CuO doping introduces a range of defect-related energy levels within the bandgap of ZnO. The presence of CuO narrows the bandgap of the nanocomposite due to the introduction of intermediate states. This modification can enhance visible light absorption and is advantageous for applications like photocatalysis and photodetectors.

The PL emission lifetime offers valuable insights into the recombination dynamics of photoexcited charge carriers. The decay behaviour of PL intensity over time can typically be modelled using an exponential function, expressed as [20]

$$I(t) = \sum_i A_i e^{-\frac{t}{\tau_i}}, \quad (5)$$

where,  $I(t)$  is the PL intensity at time  $t$ ,  $A_i$  is the amplitude associated with the  $i^{\text{th}}$  decay process and  $\tau_i$  is the lifetime associated with the  $i^{\text{th}}$  decay process. The average PL lifetime ( $\tau$ ) can be defined as [21]

$$\tau = \frac{\sum_i A_i \tau_i^2}{\sum_i A_i \tau_i}. \quad (6)$$

The calculated value of  $\tau$  is 438 ns. This indicates that the radiative recombination processes are relatively efficient in the prepared nanoparticles. The longer  $\tau$  confirms that non-radiative pathways (such as defect states or surface recombination) are not dominant and it reflects the quality of the NCs [21]. Therefore, these NCs can be considered for optoelectronic applications. Fig. 6(b) depicts the CIE-1931 chromaticity diagram for the ZnO/CuO NCs, showing its emission coordinates within the visible spectrum. The CIE-1931 diagram maps all perceivable colours as a function of two chromaticity coordinates, the  $x$  and  $y$  coordinates are 0.218 and 0.168 respectively. The black triangle marker corresponds to the chromaticity coordinates of the ZnO/CuO nanocomposite’s PL emission. The marker is located closer to the region where blue and pink/violet hues converge, suggesting that the combined emission from the material results in this perceived colour.

Colour purity (CP) is a measure of how close the chromaticity of a light source is to the dominant wavelength, and it determines the degree of saturation of the emitted colour. The concept is based on the CIE 1931 chromaticity diagram, which defines the relationship between chromaticity coordinates ( $x$ ,  $y$ ) and colour perception. The colour purity can be defined as the ratio of the distance between the chromaticity point of the light source and the reference point (usually white light) to the distance between the dominant wavelength and the reference point. It can be expressed as [22]

$$\text{CP} = \frac{\sqrt{(x - x_w)^2 + (y - y_w)^2}}{\sqrt{(x_d - x_w)^2 + (y_d - y_w)^2}} \times 100\%, \quad (7)$$

where,  $x_w$ ,  $y_w$  are the chromaticity coordinates of the reference white point and  $x_d$ ,  $y_d$  are the chromaticity coordinates of the dominant wavelength. The numerator of the Eq. (5) represents the distance between the chromaticity of the light source and the white point. It shows how far the light source deviates from neutral (white light). Whereas the

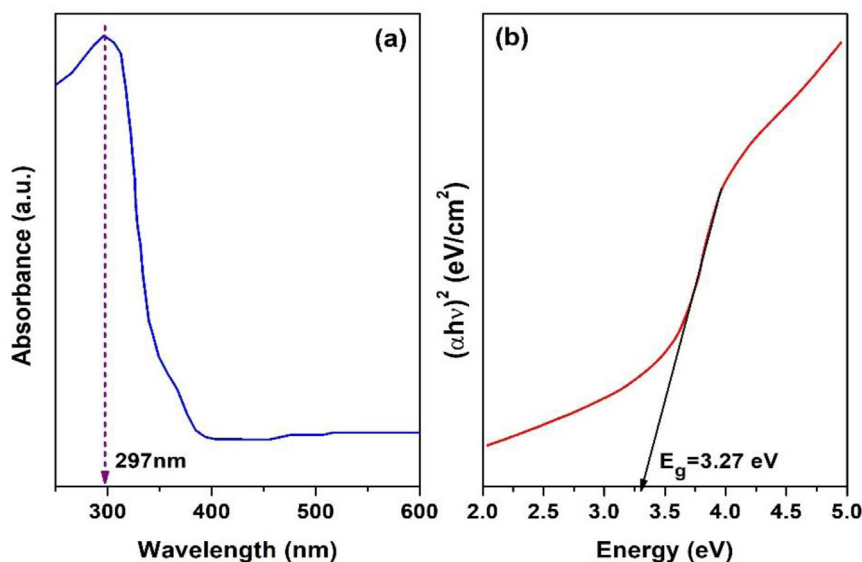


Fig. 5. (a) UV-Vis absorbance spectrum and (b) Tauc plot for ZnO/CuO NCs.

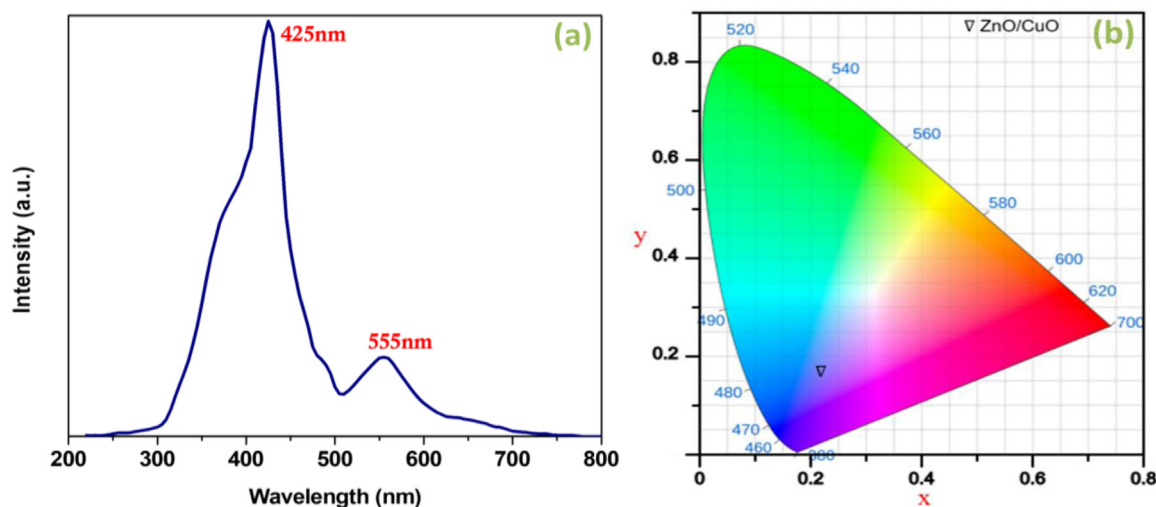


Fig. 6. (a) PL spectrum and (b) CIE diagram of ZnO/CuO NCs.

Table 3

The colour purity values for ZnO/CuO NCs.

Source	A	B	C	D50	D55	D65	D75	D93	E	F1	F2
CP (%)	67.97	58.67	51.26	58.23	56.28	52.90	50.11	<b>46.30</b>	55.10	53.80	61.35
Source	F3	F4	F5	F6	F7	F8	F9	F10	F11	F12	LED-B1
CP (%)	64.95	67.36	54.69	62.56	52.95	58.26	61.35	58.36	62.07	67.19	68.50
Source	LED-B2	LED-B3	LED-B4	LED-B5	LED-BH1	LED-RGB1	LED-V1	LED-V2			
CP (%)	66.99	61.43	57.29	52.24	67.93	68.90	<b>70.03</b>	61.92			

denominator of the Eq. (5) represents the maximum possible distance from the white point to the chromaticity of the dominant wavelength. The ratio gives the relative saturation of the colour. A light source with chromaticity coordinates close to the dominant wavelength will have a high CP value, indicating a saturated and vivid colour. If the chromaticity coordinates are closer to the white point, the CP value will be lower, indicating a more desaturated appearance. Table 3 presents data on CP for various light sources, including standard illuminants (A, B, C, D-series, and E), fluorescent lamps (F-series), and LED light sources. Among the standard illuminants, source D93 has the lowest colour purity (46.30%), indicating that it produces light with less vividness or saturation compared to other sources like A (67.97%) or B (58.67%).

These differences reflect variations in their spectral distributions, with sources like D93 often simulating cooler light with higher blue content, which can appear less saturated. Among fluorescent lamps, F12 and F3 show relatively high color purity values (67.19% and 64.95%, respectively), indicating better saturation. On the other hand, F5 (54.69%) and F7 (52.95%) exhibit lower CP values, suggesting these lamps emit light with less saturated colors. Fluorescent lamps typically show variation in CP due to differences in phosphor coatings, which affect the light's chromaticity and spectral output. Among LED sources, LED-V1 has the highest colour purity value (70.03%), followed by LED-RGB1 (68.90%). These values suggest that modern LED technologies, particularly RGB-based systems, can achieve highly saturated colours. By con-

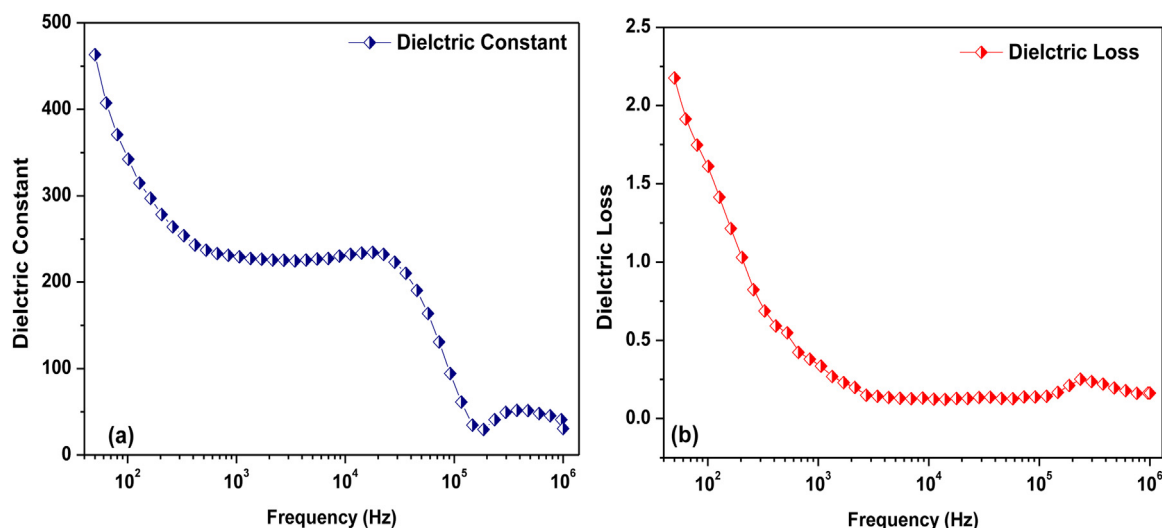


Fig. 7. The variation of (a) dielectric constant and (b) dielectric loss as a function of frequency for ZnO/CuO NCs.

trast, sources like LED-B5 (52.24%) and LED-B4 (57.29%) exhibit lower CP values, reflecting the influence of specific LED designs and phosphor layers used to produce the light. The ZnO/CuO nanocomposite's moderate CP arises from its broad and hybrid emission spectrum, making it suitable for applications requiring both tuneable chromaticity and balanced colour rendering, such as decorative lighting or optoelectronics.

### 3.6. Dielectric properties

The complex dielectric permittivity ( $\epsilon^*$ ) of a material is defined by the following Equation [23].

$$\epsilon^* = \epsilon' - j\epsilon'' \quad (8)$$

where  $\epsilon'$  and  $\epsilon''$  are real and imaginary part of permittivity. The  $\epsilon'$  is referred to as the dielectric constant, indicating the material's energy storage ability. The  $\epsilon''$  implies the energy dissipated in the dielectric material known as dielectric loss. Figs. 7(a)(b) depicts the dielectric constant and dielectric loss for ZnO/CuO NCs respectively. Both  $\epsilon'$  and  $\epsilon''$  exhibit conventional trend as they decrease with increasing F. At lower F, the higher  $\epsilon'$  is due to interfacial polarization caused by interfaces like material-electrode, material-impurities, or grain boundaries. These interfaces accumulate charges, creating potential barriers and resulting in higher  $\epsilon'$  at lower frequencies [24]. As F increases, the  $\epsilon'$  decreases rapidly due to the relaxation of extrinsic factors and the dominance of intrinsic factors in the high-F domain. This behaviour is known as Maxwell–Wagner polarization [25].

Fig. 7(b) illustrates the decreasing trend of dielectric loss with increasing F. This behaviour is primarily attributed to polarization mechanisms and relaxation dynamics within the ZnO/CuO NCs. At lower frequencies, dipoles have sufficient time to reorient in response to the slowly varying external alternating electric field, resulting in higher energy dissipation due to increased dielectric loss [26]. As the F increases, the electric field reverses direction more rapidly, making it difficult for the dipoles to realign in time. This lag in response reduces energy dissipation, thereby lowering the dielectric loss at higher frequencies.

The impedance spectra of the CuO/ZnO NCs, as depicted in the Fig. 8(a), illustrate the variation of both the real ( $Z'$ ) and imaginary ( $Z''$ ) components of impedance with frequency. At lower frequencies, both  $Z'$  and  $Z''$  exhibit high values, indicating that the material exhibits significant resistance and polarization effects in this range [27]. As the frequency increases,  $Z'$  and  $Z''$  gradually decrease, eventually becoming almost independent of frequency at higher frequencies, suggesting a decrease in resistive and capacitive contributions due to reduced interfacial polarization and enhanced charge carrier mobility [28]. The

Table 4

Equivalent electric circuit parameters from Nyquist plot.

NPs	$R_{gb}(\Omega)$	$R_b(\Omega)$	$C_{gb}(F)$	$C_b(F)$
ZnO/CuO NCs	$3.15 \times 10^6$	$8.57 \times 10^7$	$3.10 \times 10^{-15}$	$1 \times 10^{-11}$

imaginary component  $Z''$  reaches a peak at approximately 200 Hz, signifying the characteristic relaxation frequency associated with the dielectric response of the composite. The presence of this peak suggests that at this frequency, the material undergoes a transition where energy dissipation due to relaxation mechanisms is maximized [29].

Fig. 8(b) shows Nyquist plot, which displays a semicircular nature, characteristic of a single relaxation process associated with the material's charge transport properties. The semicircle implies the dominance of a parallel RC circuit behaviour, where the intercept at higher  $Z'$  values corresponds to bulk resistance, and the curvature reflects capacitive and interfacial polarization effects [30]. The impedance response of NCs is fitted using an equivalent circuit model using EIS spectrum analyzer software, shown in the inset of Fig. 8(b). The equivalent electric circuit (EEC) consisting of two parallel resistor–capacitor (RC) elements in series, representing the grain (bulk) and grain boundary contributions. Table 4 summarizes the extracted parameters from fitting with EIS Spectrum Analyzer. The fitted parameters suggest that the bulk (grain) region offers a substantially larger resistance ( $R_b$ ) and a much higher effective capacitance ( $C_b$ ) than the grain boundaries. The large  $C_b$  indicates stronger charge storage or polarization within grains, while the much smaller  $C_{gb}$  reflects limited charge accumulation at grain interfaces.

The electric modulus spectra of the CuO/ZnO NCs are shown in the Fig. 9. This illustrates the variation of the real ( $M'$ ) and imaginary ( $M''$ ) components of the modulus with F.  $M'$  exhibit a peak at ~200 Hz and  $M''$  at 4.3 kHz. The increase and decrease of electric modulus with F suggest that at lower frequencies, long-range mobility of charge carriers dominates, leading to negligible contribution to the modulus. As the frequency increases, the relaxation process becomes more prominent, causing  $M'$  to increase, followed by a decrease due to the reduction in polarization effects at high frequencies. The peak represents the characteristic relaxation process of the material. The peak is associated with charge carrier hopping and localized motion, reflecting the transition from long-range to short-range mobility [31]. The observed peaks in both  $M'$  and  $M''$  confirm the presence of a dielectric relaxation mechanism.

The AC conductivity ( $\sigma_{ac}$ ) spectrum of the CuO/ZnO NCs, as shown in the Fig. 10, exhibits F-dependent behaviour and follows Jonscher's

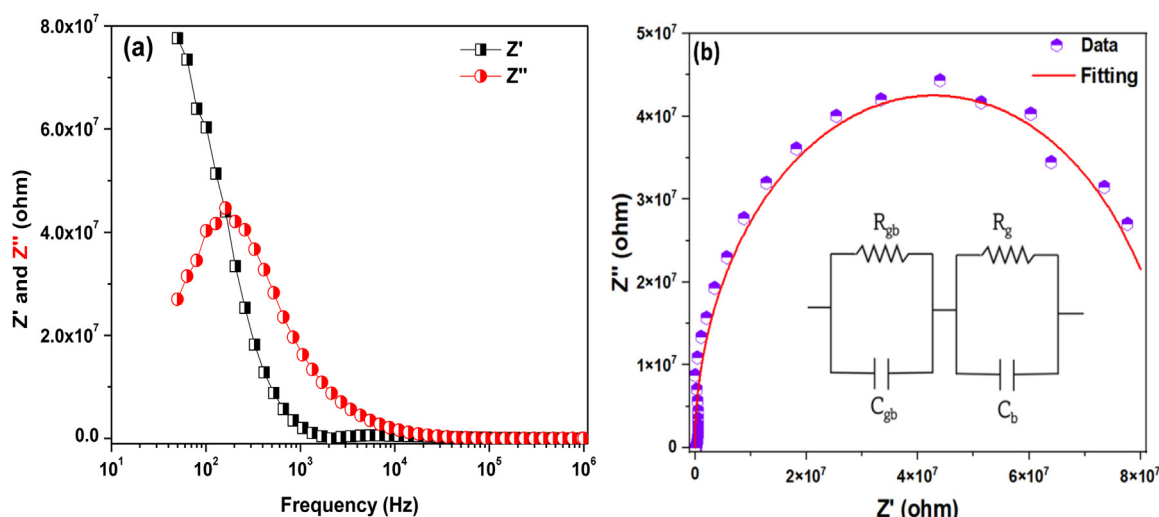


Fig. 8. (a) The variation of impedance as function of frequency and (b) Nyquist plot with equivalent circuit for ZnO/CuO NCs.

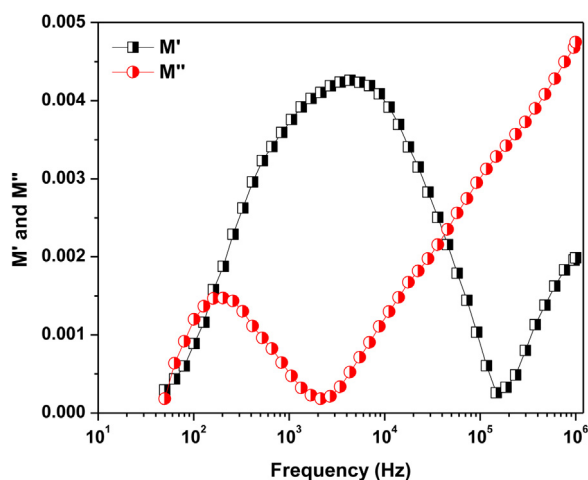


Fig. 9. The variation of electric modulus as a function of frequency for CuO/ZnO NCs.

universal power law. At lower frequencies, the conductivity remains nearly constant, indicating the dominance of DC conductivity ( $\sigma_{dc}$ ), which arises from long-range charge transport. As  $F$  increases,  $\sigma_{ac}$  increases significantly, following a power-law behaviour, which indicates a hopping conduction mechanism associated with charge carrier movement in localized states. The solid curve represents a fit to Jonscher's power law, confirming that the conductivity follows the expected trend. Jonscher's universal power law is expressed as [32]

$$\sigma_{ac}(\omega) = \sigma_{dc} + A\omega^s, \quad (9)$$

where,  $A$  is a material-dependent pre-factor, and  $s$  is the frequency exponent ( $0 < s < 1$ ). The presence of a nearly constant  $\sigma_{dc}$  at low frequencies suggests that charge transport occurs via a continuous pathway, whereas the increase in  $\sigma_{ac}$  at higher frequencies is due to hopping conduction of charge carriers between localized states. The exponent  $s$  provides information about the conduction mechanism, where its value less than 1 indicates that the system follows a correlated barrier hopping (CBH) model, a common feature in disordered semiconductors [33]. The observed increase in  $\sigma_{ac}$  with  $F$  suggests that at higher frequencies, the hopping of charge carriers between defect states or localized sites becomes more dominant. The excellent fit of the experimental data with Jonscher's power law further confirms the reliability of the observed

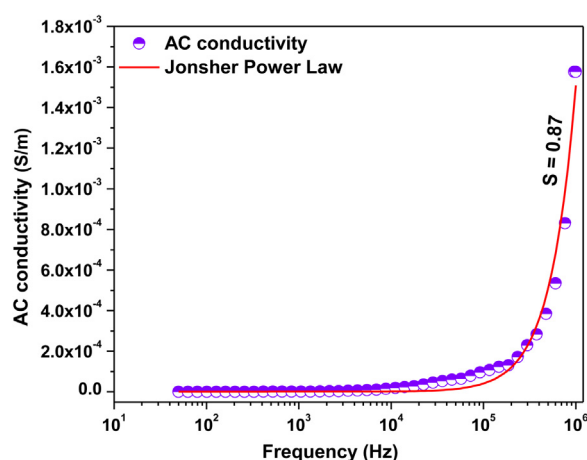


Fig. 10. The variation of AC conductivity as a function of frequency for CuO/ZnO NCs.

trend and supports the role of  $F$ -dependent charge carrier dynamics in the CuO/ZnO NCs.

### 3.7. Photocatalytic studies

Fig. 11 highlights the influence of pH on the photocatalytic degradation efficiency of ZnO/CuO NCs, studied over a pH range of 2 to 10 using a dye concentration of 0.5 mg/L for a reaction time of 60 min. The pH of the dye solution is a critical parameter in photocatalytic degradation due to its significant impact on the surface charge properties of the catalyst and the generation of reactive oxidative species [34]. The ZnO/CuO NCs exhibit a point of zero charge ( $pH_{zpc}$ ) of 7.8, consistent with literature [35]. This suggests that the catalyst surface becomes positively charged in acidic conditions ( $pH = 2-7$ ) and negatively charged under alkaline conditions ( $pH = 7-10$ ). At neutral pH ( $pH = 7$ ), the maximum degradation efficiency of CV dye was observed, reaching up to 83%. At  $pH = 7$ , the surface of the ZnO/CuO NCs remains protonated and positively charged, which facilitates better interaction with the negatively charged dye molecules, enhancing degradation efficiency. Positive holes ( $h^+$ ) act as strong oxidizing agents at  $pH = 7$ . The high redox potential of photo-generated holes in the valence band of the NCs is sufficient to generate hydroxyl radicals, which are key contributors to dye degradation. NCs function as an efficient photosensitizer, absorbing light energy and enhancing charge separation for improved photocatalytic activity.

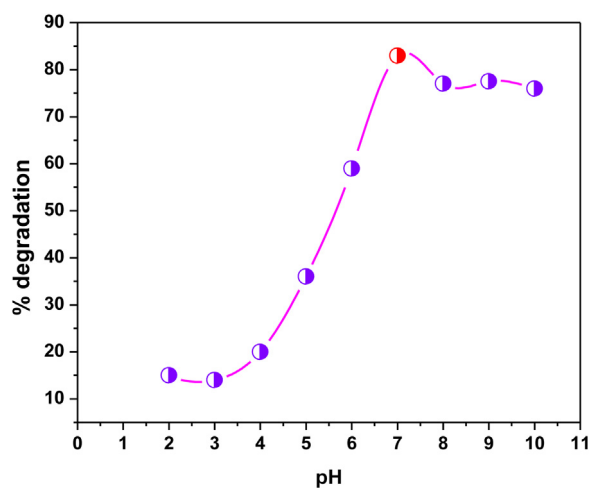


Fig. 11. Influence of pH on photocatalytic degradation of CV by ZnO/CuO NCs.

In addition to hydroxyl radical generation, direct oxidation of the CV dye occurs as dye molecules interact with the positive holes on the catalyst surface [36]. Under acidic conditions ( $\text{pH} < 7$ ), electrostatic repulsion between positively charged catalyst surfaces and dye molecules may reduce degradation efficiency. Conversely, at alkaline conditions ( $\text{pH} > 7$ ), the reduced availability of protonated surface sites and competitive adsorption of hydroxyl ions ( $\text{OH}^-$ ) can hinder photocatalytic performance [37].

The effect of varying the initial concentration of CV dye on the photocatalytic degradation efficiency of the ZnO/CuO NCs was investigated at  $\text{pH} = 7$ , with concentrations ranging from 0 to 1 mg/L. The results, illustrated in Fig. 12, shows a decline in degradation efficiency as the dye concentration increased. At lower concentrations, the catalyst surface has abundant active sites available for the adsorption of dye molecules and efficient absorption of incident photons. This promotes the formation of reactive hydroxyl radicals, the primary agents responsible for breaking down dye molecules during photocatalytic reactions [38]. However, as the dye concentration increases, the surface of the catalyst becomes saturated with dye molecules. This saturation impedes light penetration, as the dye molecules themselves begin to absorb significant portions of the incident radiation, reducing the energy available for photocatalytic activity. Also, the generation of hydroxyl radicals is hindered at higher dye concentrations due to the occupation of active surface sites by excess dye molecules. The limited availability of these radicals, combined with their inherently short lifespan, exacerbates the challenge. Effective collisions between hydroxyl radicals and dye molecules become less frequent, further diminishing the degradation efficiency [39]. Along with these, the accumulation of dye intermediates and byproducts during the reaction can contribute to surface fouling, which further inhibits light absorption and active site availability. The reduced degradation efficiency at higher concentrations highlights the importance of optimizing dye concentrations for practical wastewater treatment applications.

The effect of catalyst loading on the photocatalytic degradation of CV was examined by varying the ZnO/CuO NCs concentration from 0 to 1.0 g/L under identical conditions ( $\text{pH} = 7$ , fixed dye concentration and 60 min irradiation). As shown in Fig. 13(a), which illustrates the degradation efficiency as a function of catalyst dose, the efficiency increased steadily and reached a maximum at 1.0 g/L. This trend is attributed to the larger number of active sites available at higher loadings, which enhances dye adsorption and promotes the generation of reactive species (e.g.,  $\bullet\text{OH}$  radicals) under UV-Vis irradiation, thereby accelerating the degradation process.

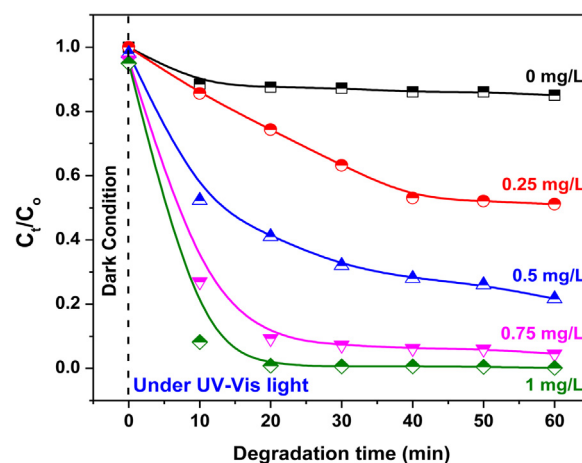


Fig. 12. Effect of initial dye concentration on the photocatalytic degradation of CV.

The UV-Vis absorption spectra, monitored over a time period of 0 to 60 min and shown in Fig. 13(b). The degradation rate increased with dye concentration up to  $\sim 0.5$ – $1.0$  mg/L, which is due to the greater number of dye molecules available for adsorption and reaction on the catalyst surface. However, at higher concentrations, the efficiency declined and eventually plateaued due to saturation of active sites and the light-shielding effect of excess dye molecules, which reduce photon penetration into the solution. This behaviour indicates that an optimum dye concentration exists in the range of 0.5–1.0 mg/L for effective photocatalytic performance of ZnO/CuO NCs. To further understand the reaction kinetics, the photocatalytic degradation rate constant ( $k$ ) was determined using a first-order kinetic model. The relationship between  $\ln(C_0/C_t)$  and time ( $t$ ) was plotted for all samples, with the slopes of these plots used to calculate the corresponding rate constants, as shown in Fig. 13(c). The results indicate that lower initial dye concentrations, particularly at 0.25 mg/L, exhibit the highest reaction rate constants followed pseudo-first-order kinetics with an excellent linear fit ( $R^2 \approx 0.99$ ). This can be attributed to efficient light penetration and minimal competition among dye molecules for active sites on the catalyst surface. This suggests that the photocatalytic degradation process is most effective under conditions where fewer dye molecules are present. However, at higher initial dye concentrations ( $\geq 0.5$  mg L $^{-1}$ ), deviations from linearity were observed, suggesting that the first-order model does not adequately describe the reaction.

Fig. 14(a) illustrates the photocatalytic degradation process of CV dye using a ZnO/CuO NCs under sunlight. Upon exposure to sunlight, these nanoparticles are activated, enabling the catalytic degradation process. CV, a complex organic dye interacts with the activated catalyst. As a result, the dye undergoes degradation, breaking down into smaller fragments. Fig. 14(b) gives schematic representation of the underlying mechanisms in the photocatalytic reaction. When exposed to sunlight, photons with energy equal to or greater than the band gap energy ( $E_g$ ) excite electrons from the VB to CB of the semiconductor catalyst. This process creates electron-hole pairs ( $e^-$  and  $h^+$ ). The electrons in CB can reduce oxygen molecules ( $\text{O}_2$ ) to form reactive oxygen species such as superoxide anions ( $\text{O}_2^{\bullet-}$ ). Meanwhile, the positive holes ( $h^+$ ) in VB oxidize water molecules or hydroxide ions ( $\text{OH}^-$ ) to generate highly reactive hydroxyl radicals ( $\text{OH}\bullet$ ). These reactive species, superoxide anions and hydroxyl radicals are powerful oxidizing agents that break down organic pollutants, CV dye, into such as carbon dioxide ( $\text{CO}_2$ ) and water ( $\text{H}_2\text{O}$ ). The depiction of recombination processes between electrons and holes signifies a competing mechanism that can reduce the efficiency of photocatalytic reactions.

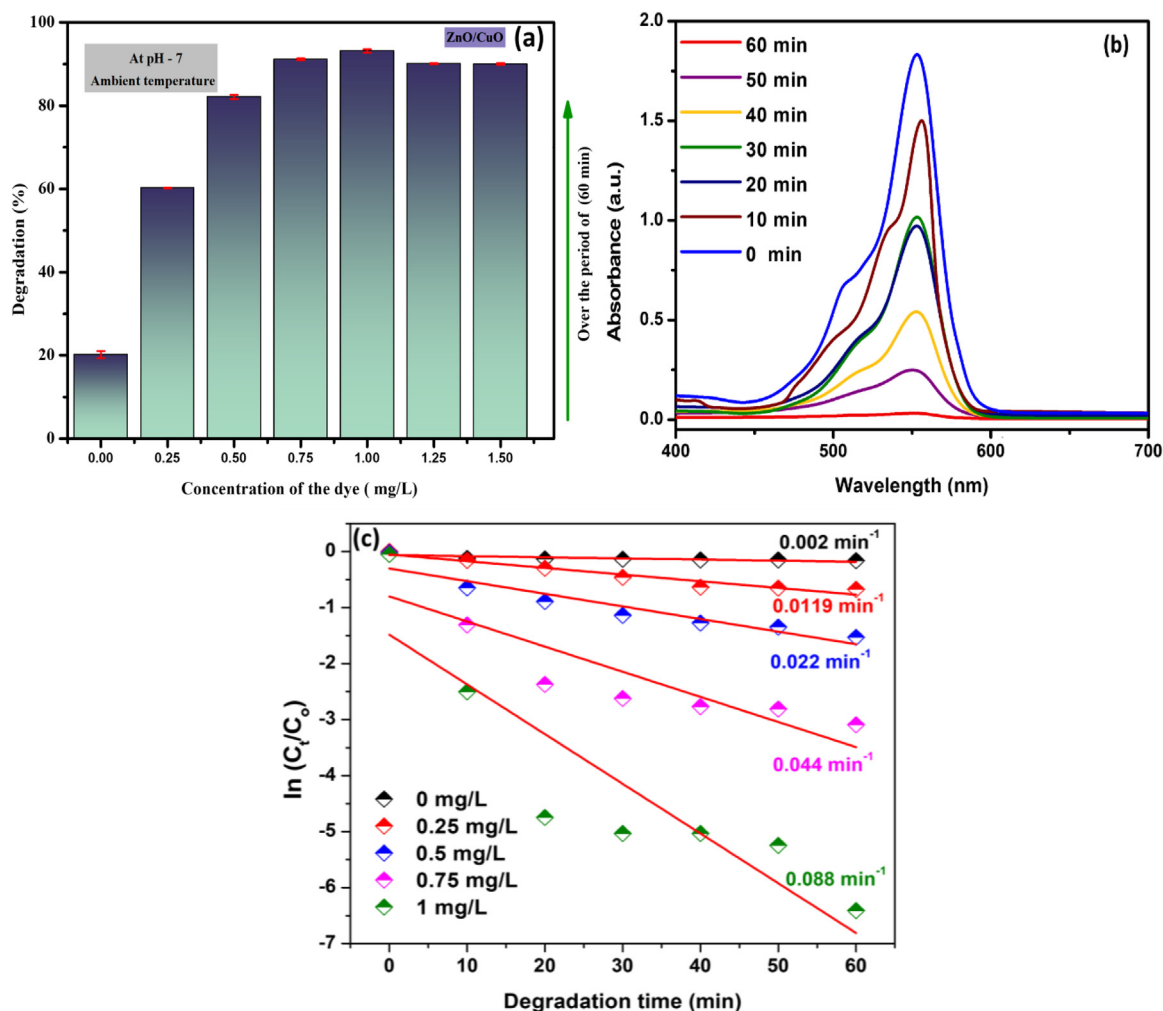


Fig. 13. (a): Effect of catalyst dose on the photocatalytic degradation of CV, (b) UV-Vis spectral variation during CV degradation and (c) Kinetics study ( $\ln(C_0/C_t)$  vs.  $t$ ).

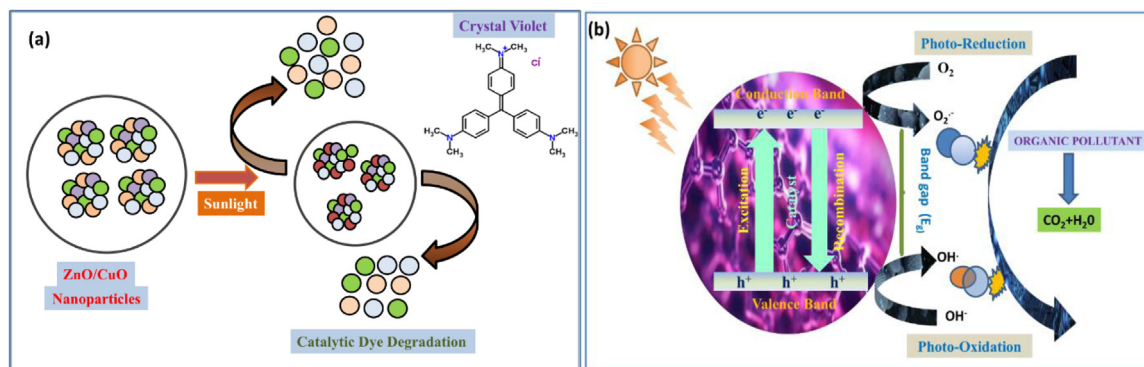


Fig. 14. (a) The photocatalytic degradation process of CV dye using ZnO/CuO NCs and (b) Photocatalytic mechanism.

#### 4. Conclusion

The structural, optical, dielectric, and photocatalytic properties of ZnO/CuO NCs synthesized via a green solution combustion method were comprehensively analyzed. XRD analysis confirmed the formation of hexagonal ZnO and monoclinic CuO phases. SEM images revealed agglomerated particles with a rough and porous morphology, advantageous for photocatalysis. The optical bandgap was determined to be 3.27 eV, while PL analysis showed strong emissions at 425 nm (NBE) and

555 nm (defect states), highlighting their optoelectronic potential. The ZnO/CuO NCs exhibited a moderate colour purity of 70.03% for LED-V1 source, making it suitable for lighting applications. Dielectric studies demonstrated a high dielectric constant and minimal energy dissipation, confirming superior charge storage capabilities. Photocatalytic degradation of crystal violet dye reached 83% efficiency at pH = 7, with optimal catalyst loading of 1.0 g/L. These results evident that the ZnO/CuO NCs are promising materials for energy storage, environmental remediation, and optoelectronic applications.

## Declaration of Competing Interest

The authors declare that they have no known competing financial interests or personal relationships that could have appeared to influence the work reported in this paper.

## CRedit authorship contribution statement

**Sahana Nagarakere Chandranna:** Writing – review & editing, Validation, Methodology, Investigation. **Vinayakprasanna N Hegde:** Writing – review & editing, Writing – original draft, Investigation, Formal analysis, Conceptualization. **N C Sandhya:** Writing – review & editing, Methodology, Investigation, Data curation. **B C Hemaraju:** Formal analysis, Validation, Writing – review & editing. **Pradeep T M:** Writing – review & editing, Visualization.

## References

- [1] A. Saka, L. Tesfaye, K. Ramaswamy, Synthesis, characterization, and applications of ZnO, Ag<sub>2</sub>O, and ZnO/Ag<sub>2</sub>O nanocomposites: A review, *Adv. Cond. Matter. Phys.* 2024 (2024) 5755167, doi:10.1155/2024/5755167.
- [2] V.N. Hegde, V.V. M, P.T. M, H.B. C, Study on structural, morphological, elastic and electrical properties of ZnO nanoparticles for electronic device applications, *Adv. Mater. Dev.* 9 (2024) 100733, doi:10.1016/J.JSAM.2024.100733.
- [3] J. Fang, H. Fan, Y. Ma, Z. Wang, Q. Chang, Surface defects control for ZnO nanorods synthesized by quenching and their anti-recombination in photocatalysis, *Appl. Surf. Sci.* 332 (2015) 47–54, doi:10.1016/J.APSUSC.2015.01.139.
- [4] S. Akter, T.T. Sikdar, M. Sultana, S. Ahmed, M.S. Bashar, M.K. Rahman, Enhancing the performance of CuO thin film in solar cell by introducing optimum amount of Ni doping, *J. Mater. Sci.* 35 (2024) 1299, doi:10.1007/s10854-024-13053-x.
- [5] M. Advaita, K. Mahendra, J. Pattar, P.P. Das, Synthesis of ZnO and CuO–ZnO nanocomposites for photo-conducting and dielectric applications, *Mater. Chem. Phys.* 322 (2024) 129545, doi:10.1016/J.MATCHEMPHYS.2024.129545.
- [6] K.S. Mamatha, H.M. Suresh Kumar, T.D. Puttaraju, T.L. Soundarya, G. Nagaraju, Eco-inspired synthesis of ZnO/CuO nanocomposites using *Phyllanthus niruri*: Unveiling superior photocatalytic, antibacterial efficacy against *Escherichia coli* and *Staphylococcus aureus*, and latent fingerprint studies, *Ionics* 30 (2024) 7665–7684, doi:10.1007/s11581-024-05823-8/FIGURES/18.
- [7] D. Yadav, P.S. Shukla, G.D. Varma, Synthesis of rGO-CuO/ZnO nanocomposites for humidity tolerant room temperature NO<sub>2</sub> gas sensor, *Appl. Phys. A* 130 (2024) 713, doi:10.1007/s00339-024-07891-z.
- [8] T. Chang, Z. Li, G. Yun, Y. Jia, H. Yang, E. Photocatalytic, enhanced photocatalytic activity of ZnO/CuO nanocomposites synthesized by hydrothermal method, *Nano-Micro Lett.* 5 (2013) 163–168, doi:10.1007/BF03353746.
- [9] R. Saravanan, S. Karthikeyan, V.K. Gupta, G. Sekaran, V. Narayanan, A. Stephen, Enhanced photocatalytic activity of ZnO/CuO nanocomposite for the degradation of textile dye on visible light illumination, *Mater. Sci. Eng.: C* 33 (2013) 91–98, doi:10.1016/J.MSEC.2012.08.011.
- [10] R.S. Shinde, S.D. Khairnar, M.R. Patil, V.A. Adole, P.B. Koli, V.V. Deshmane, D.K. Halwar, R.A. Shinde, T.B. Pawar, B.S. Jagdale, A.V. Patil, Synthesis and characterization of ZnO/CuO nanocomposites as an effective photocatalyst and gas sensor for environmental remediation, *J. Inorg. Organomet. P.* 32 (2022) 1045–1066, doi:10.1007/S10904-021-02178-9.
- [11] N. Doebelin, R. Kleeberg, Profex: A graphical user interface for the Rietveld refinement program BGMN, *J. Appl. Cryst.* 48 (2015) 1573–1580, doi:10.1107/S1600576715014685.
- [12] F.T.L. Muniz, M.A.R. Miranda, C. Morilla Dos Santos, J.M. Sasaki, The Scherrer equation and the dynamical theory of X-ray diffraction, *Acta Cryst.* 72 (2016) 385–390, doi:10.1107/S205327331600365X.
- [13] V. Mote, Y. Purushotham, B. Dole, Williamson-Hall analysis in estimation of lattice strain in nanometer-sized ZnO particles, *J. Theor. Appl. Phys.* 6 (2012) 6, doi:10.1186/2251-7235-6-6.
- [14] G.A. Rance, D.H. Marsh, S.J. Bourne, T.J. Reade, A.N. Khlobystov, Van der Waals interactions between nanotubes and nanoparticles for controlled assembly of composite nanostructures, *ACS Nano* 4 (2010) 4920–4928, doi:10.1021/NN101287U/SUPPL\_FILE/NN101287U\_SI\_001.PDF.
- [15] S. Mandal, S. Basak, P. Kumar, B. Satpathy, S. Das, K. Das, CTAB-facilitated ex-situ synthesis of chitosan-based ZnO, CuO, and ZnO/CuO nanocomposites for improved optical emission, *Opt. Mater.* 155 (2024) 115813, doi:10.1016/J.OPTMAT.2024.115813.
- [16] K. Mubeen, A. Irshad, A. Safeen, U. Aziz, K. Safeen, T. Ghani, K. Khan, Z. Ali, I. ul Haq, A. Shah, Band structure tuning of ZnO/CuO composites for enhanced photocatalytic activity, *J. Saudi Chem. Soc.* 27 (2023) 101639, doi:10.1016/J.JSCS.2023.101639.
- [17] N.L. Kazanskiy, M.A. Butt, S.N. Khonina, Silicon photonic devices realized on refractive index engineered subwavelength grating waveguides-A review, *Opt. Laser Technol.* 138 (2021) 106863, doi:10.1016/J.OPTLASTEC.2020.106863.
- [18] R.R. Reddy, Y. Nazeer Ahammed, K. Rama Gopal, D.V. Raghuram, Optical electronegativity and refractive index of materials, *Opt. Mater.* 10 (1998) 95–100, doi:10.1016/S0925-3467(97)00171-7.
- [19] V.A. Fonoberov, K.A. Alim, A.A. Balandin, F. Xiu, J. Liu, Photoluminescence investigation of the carrier recombination processes in ZnO quantum dots and nanocrystals, *Phys. Rev. B Condens. Matter. Mater. Phys.* 73 (2006) 165317, doi:10.1103/PHYSREVB.73.165317/FIGURES/8/THUMBNAI.
- [20] R. Chen, Apparent stretched-exponential luminescence decay in crystalline solids, *J. Lumin.* 102–103 (2003) 510–518, doi:10.1016/S0022-2313(02)00601-4.
- [21] Y. Zhong, A.B. Djurišić, Y.F. Hsu, K.S. Wong, G. Brauer, C.C. Ling, W.K. Chan, Exceptionally long exciton photoluminescence lifetime in ZnO tetrapods, *J. Phys. Chem. C* 112 (2008) 16286–16295, doi:10.1021/JP804132U.
- [22] D. Sahu, A. Verma, D.P. Bisen, N. Brahme, C. Belodhiya, K. Tiwari, A. Sahu, Investigation of photoluminescence and thermoluminescence properties of UV&gamma irradiated Li<sub>4</sub>SrCa(SiO<sub>4</sub>)<sub>2</sub>:dy<sup>3+</sup> phosphor, *J. Mater. Sci.* 35 (2024) 527, doi:10.1007/s10854-024-12287-z.
- [23] V.N. Hegde, Structural, dielectric, and optoelectronic properties of green synthesized NiO nanoparticles, *Mater. Chem. Phys.* 333 (2025) 130319, doi:10.1016/J.MATCHEMPHYS.2024.130319.
- [24] M. Jebli, N. Hamdaoui, J. Dhahri, M. Ben Henda, M.L. Bouazizi, A. Hamdi, Analysis of the structural characterization, electric transport, and dielectrical relaxation behavior of Ba<sub>0.97</sub>La<sub>0.02</sub>Ti<sub>0.95</sub>Nb<sub>0.04</sub>O<sub>3</sub> electronic ceramic, *J. Inorg. Organomet. Polym. Mater.* 32 (2022) 1766–1777, doi:10.1007/S10904-021-02215-7/METRICS.
- [25] B. Wang, H. Wu, W. Hou, Z. Fang, H. Liu, F. Huang, S. Li, H. Zhang, Optimizing dielectric polarization for electromagnetic wave attenuation via an enhanced Maxwell–Wagner–Sillars effect in hollow carbon microspheres, *J. Mater. Chem. A* 11 (2023) 23498–23510, doi:10.1039/D3TA05647C.
- [26] M. Samet, V. Levchenko, G. Boiteux, G. Seytre, A. Kallel, A. Serghei, Electrode polarization vs. Maxwell–Wagner–Sillars interfacial polarization in dielectric spectra of materials: characteristic frequencies and scaling laws, *J. Chem. Phys.* 142 (2015) 194703, doi:10.1063/1.4919877.
- [27] S. Huang, K. Liu, W. Zhang, B. Xie, Z. Dou, Z. Yan, H. Tan, C. Samart, S. Kongparakul, N. Takesue, H. Zhang, All-organic polymer dielectric materials for advanced dielectric capacitors: Theory, property, modified design and future prospects, *Polym. Rev.* 63 (2023) 515–573, doi:10.1080/15583724.2022.2129680.
- [28] M.I. Mohammed, Dielectric dispersion and relaxations in (PMMA/PVDF)/ZnO nanocomposites, *Polym. Bull.* 79 (2022) 2443–2459, doi:10.1007/S00289-021-03606-Z/FIGURES/12.
- [29] R. Tang, C. Jiang, W. Qian, J. Jian, X. Zhang, H. Wang, H. Yang, Dielectric relaxation, resonance and scaling behaviors in Sr<sub>3</sub>Co<sub>2</sub>Fe<sub>24</sub>O<sub>41</sub> hexaferrite, *Sci. Rep.* 5 (2015) 13645, doi:10.1038/srep13645.
- [30] M.V. Jacob, S. Thomas, M.T. Sebastian, J. Honkama, H. Jantunen, Frequency and temperature dependent dielectric properties of CuO nanoparticles, *Chem. Phys. Impact* 8 (2024) 100474, doi:10.1016/J.CHPHI.2024.100474.
- [31] V.N. Hegde, V.V. Manju, B.C. Hemaraju, Frequency and temperature dependent dielectric properties of CuO nanoparticles, *Chem. Phys. Impact* 8 (2024) 100474, doi:10.1016/J.CHPHI.2024.100474.
- [32] B.M. Greenhoe, M.K. Hassan, J.S. Wiggins, K.A. Mauritz, Universal power law behavior of the AC conductivity versus frequency of agglomerate morphologies in conductive carbon nanotube-reinforced epoxy networks, *J. Polym. Sci. B Polym. Phys.* 54 (2016) 1918–1923, doi:10.1002/POLB.24121.
- [33] S.F. Chérif, A. Chérif, W. Dridi, M.F. Zid, AC conductivity, electric modulus analysis, dielectric behavior and bond valence sum analysis of Na<sub>3</sub>Nb<sub>4</sub>As<sub>2</sub>O<sub>19</sub> compound, *Arab. J. Chem.* 13 (2020) 5627–5638, doi:10.1016/J.ARABJC.2020.04.003.
- [34] S.A. Ahire, P.B. Koli, A.V. Patil, B.S. Jagdale, A.A. Bachhav, T.B. Pawar, Designing of screen-printed stannous oxide (SnO<sub>2</sub>) thick film sensors modified by cobalt and nitrogen elements for sensing some toxic gases and volatile organic compounds, *Curr. Res. Green Sustain. Chem.* 4 (2021) 100213, doi:10.1016/J.CRGC.2021.100213.
- [35] S.D. Khairnar, V.S. Shrivastava, Photocatalytic degradation of chlorpyrifos and methylene blue using α-Bi<sub>2</sub>O<sub>3</sub> nanoparticles fabricated by sol–gel method, *SN. Appl. Sci.* 1 (2019) 1–10, doi:10.1007/S42452-019-0761-4/FIGURES/11.
- [36] A. Nezamzadeh-Ejehieh, M. Karimi-Shamsabadi, Decolorization of a binary azo dyes mixture using CuO incorporated nanozeolite-X as a heterogeneous catalyst and solar irradiation, *Chem. Eng. J.* 228 (2013) 631–641, doi:10.1016/J.CEJ.2013.05.035.
- [37] M.R. Patil, S.D. Khairnar, V.S. Shrivastava, Synthesis, characterisation of polyaniline–Fe<sub>3</sub>O<sub>4</sub> magnetic nanocomposite and its application for removal of an acid violet 19 dye, *Appl. Nanosci.* 6 (2016) 495–502, doi:10.1007/S13204-015-0465-Z/TABLES/1.
- [38] A. Nezamzadeh-Ejehieh, M. Khorsandi, Photodecolorization of eriochrome Black T using NiS–P zeolite as a heterogeneous catalyst, *J. Hazard. Mater.* 176 (2010) 629–637, doi:10.1016/J.JHAZMAT.2009.11.077.
- [39] S.D. Khairnar, A.N. Kulkarni, S.G. Shinde, S.D. Marathe, Y.V. Marathe, S.D. Dhole, V.S. Shrivastava, Synthesis and characterization of 2-D La-doped Bi<sub>2</sub>O<sub>3</sub> for photocatalytic degradation of organic dye and pesticide, *J. Photochem. Photobiol.* 6 (2021) 100030, doi:10.1016/J.JPAP.2021.100030.